HACKING THE BRAIN: OPPORTUNITIES IN SOFT WIRELESS BIOELECTRONICS

An Undergraduate Research Scholars Thesis

by

STEPHANIE WILCOX

Submitted to the Undergraduate Research Scholars program at
Texas A&M University
in partial fulfillment of the requirements for the designation as an

UNDERGRADUATE RESEARCH SCHOLAR

Approved by Research Advisor: Dr. Sung Il Park

May 2018

Major: Electrical Engineering

TABLE OF CONTENTS

Page

ABSTRACT 1

ACKNOWLEDGMENTS 3

NOMENCLATURE 4

CHAPTER

I. INTRODUCTION 5

II. METHODS 8

RF Power Supply and Multichannel Stretchable Antenna 8
Device Fabrication 8
Single-Channel Light Emitting Device 9
Multi-Channel Light Emitting Device 13

III. RESULTS 15

Optimization of Single-Channel Device 15
Transmitting and Receiving Antenna Characterization 26
LED Control System for Multi-Channel Device 28

IV. DISCUSSION 29

V. CONCLUSION 30

REFERENCES 32

ABSTRACT

Hacking the Brain: Opportunities in Soft Wireless Bioelectronics

Stephanie Wilcox
Department of Electrical and Computer Engineering
Texas A&M University

Research Advisor: Dr. Sung Il Park
Department of Electrical and Computer Engineering
Texas A&M University

Traditional techniques used to determine neuron activity in cognitive function, such as penetrating or surface-mounted electrodes, severely limit the comprehensive study of the brain. Such methods confound thermal effects, lack cell-type specificity, cause long term tissue damage, and require the tethering of experimental animals. Eliminating these obstacles, wireless, in vivo optogenetic platforms increase diversity of application and experimental complexity, while enabling highly controlled targeting of regions of interest. However, current optogenetic devices are limited by size, weight, and wireless area coverage. In this study, two fully implantable, wireless devices are developed to mitigate these restrictions, a single-channel system allowing optogenetic control and a multi-channel optoelectronic system permitting both optogenetic control and monitoring of neuronal activity in vivo. Operating at wavelengths ranging from UV to blue, yellow, and red, the devices developed utilize microscale light-emitting diodes (LEDs), referred to as micro-LEDs, connected to subdermal magnetic coil antennas for optogenetic control. The resulting devices permit highly controlled stimulation or inhibition of neuronal activity spanning the dimensions of the cage environment, while remaining light-weight and power efficient. These devices permit the investigation of a

broad range of cerebral functions including migraines and psychiatric disorders, allowing for deeper understanding of mechanisms and improved treatment.

ACKNOWLEDGEMENTS

I would like to thank Dr. Park for giving me the opportunity to work in the lab and partake in such innovative and exciting research. I would also like to thank Wooseok Kim and Dong-Hyun Baek for the help and guidance during my research.

NOMENCLATURE

ChR2	Channelrhodopsin-2
dNAcSh	Dorsal nucleus accumbens shell
ILED	Inorganic Light Emitting Diode
LED	Light Emitting Diode
NAcSh	Nucleus accumbens shell
PDMS	Polydimethylsiloxane
RF	Radio frequency
vNAcSh	Ventral nucleus accumbens shell

CHAPTER I

INTRODUCTION

Understanding the functions of the brain and evaluating neural impulses comprise immense, yet rewarding challenges. An increase in understanding of the brain may permit early detection of neurodegenerative diseases, improved comprehension of neural activity, and enhanced treatment of brain diseases, improving the lives of innumerable individuals. However, current techniques limit the efficacy required as a result of adverse tissue health effects, absence of cell-type specificity, thermal effects, and the inability to target small groups of neurons in electrically conductive tissues (Aravanis AM). Devoid of these errors, optogenetic technology permits the development of minimally invasive devices to control and monitor neuronal activity through light-sensitive channels. In addition, flexible, wireless optoelectronic devices permit the free movement of animals and increase the intricacy and diversity of experiments (D. S. Sung Il Park). However, optogenetic platforms face several challenges to reach maximal experimental viability and economic feasibility.

Taking advantage of genetically engineered neurons that express light-sensitive proteins, optogenetics permits neuronal control by optogenetic actuators and the optical recording of neuronal activity through optogenetic sensors (Park, Shin and McCall). When stimulated by light of the correct frequency, optogenetic actuators activate, inhibit, or modify signal pathways dependent upon the present opsin, a naturally occurring light-sensitive protein. This modulation results from the formation of a retinal-opsin complex after binding. If a photon strikes the retinal-opsin, the retinal, a form of Vitamin A which isomerizes upon photon absorption, will induce the modification of opsin's conformation (Guru, Post and Ho). This alteration in turn produces a

change in neuronal activity (Guru, Post and Ho). Optogenetic sensors, or optical sensor proteins, monitor an array of cellular parameters including ion and metabolite concentrations, enzyme activities, and membrane voltage (Rost, Schneider-Warme and Schmitz). Upon conformational changes resulting from molecular interactions, fluorescent indicators express the alteration as a change in fluorescence spectra, fluorescence intensity, or fluorescence resonance energy transfer (Rost, Schneider-Warme and Schmitz). The result of the neuronal activity change is then measured intensiometrically or reatiometrically. Common fluorescent sensors in neuroscience include genetically encoded calcium indicators, genetically encoded voltage indicators, and pH sensors (Rost, Schneider-Warme and Schmitz).

This document describes a single-channel optoelectronic device and a multi-channel optoelectronic device. The single-channel device developed emits light from a micro-LED to alter neuronal activity. To characterize and optimize the performance of the device, several parameters including RF power magnitude, RF power frequency, capacitance, and location in the experiment cage are investigated. In addition, a multi-channel device, capable of controlled light emission from four channels, is introduced. In conjunction with stimulating the selected channel, the multi-channel device collects real-time data resulting from the neuronal activity.

The devices integrate multi-model interfaces including an optical, electrical, and chemical interface with subcortical neurons. For optogenetic modulation of subcortical neurons, micro-scale LEDs embedded in PDMS, a biocompatible silicone, produce a soft, conformal substrate for light delivery at 460 nm, the peak stimulation wavelength of opsin ChR2. In addition, the platform utilizes RF energy harvesting techniques to wirelessly power the device. Operation relies on capacitive coupling between adjacent serpentine traces within the fully

implanted device, producing sufficient power at distances of several meters from the antenna sources (D. S. Sung Il Park; G. S.-H.-I.-K. Sung Il Park).

Previous research within the Park and Dussor/Price groups exhibits the viability of multi-channel neural probes. During this experiment, preprodynorphin-IRES-cre positive mice infected with AAV5-DIO-ChR2-eYFP virus to selectively express ChR2 in dynorphinergic neurons in the NAcSh demonstrates the validity of a multi-channel operation for photostimulation of two discrete subregions in the brain (D. S. Sung Il Park). In this arrangement, vNAcSh and dNAcSh respond to different wavelengths of light emitted from micro-LEDs separated by a small distance. Building upon these findings, the previously described devices seek to contribute to the viability and complexity of optoelectronics neural interfaces.

CHAPTER II

METHODS

The development of the optoelectronic system may be separated into several components not limited to the following: 1) RF power supply unit and multichannel stretchable antenna 2) device fabrication. Following these sections, the methodology of designing and developing the single-channel device and the multi-channel device will be introduced.

RF Power Supply and Multichannel Stretchable Antenna

The RF transmission systems is composed of a single generator (N5181 MXF, Agilent), a power amplifier (1189/BBM3K5KKO, Richardson RFPD), a DC power supply (U8031A, Keysight Technologies) with a heat sink (53M7972, Fischer Elektronic), and TX antennas (PE51019-3, Pasternack Enterprices) with a splitter (RFLT4W0727GN, RFLambda). The outputs (channel 1 and 2) connect to the J3 input of the amplifier with VDD into pins 6 and 7, and GND into pins 8, 9, and to the fan. The input of the amplifier is connected to the output of the signal generator. The amplifier is then connected to the splitter to output to the TX antennas.

Device Fabrication

Device fabrication occurs in nine steps. First, a clean glass slide (75 mm long, 50 mm wide, and 1 mm thick) is coated with polymethyl methacrylate (PMMA, 495 PMMA A6, Microchem). Next, a 2 μm layer of polyimide (PI) is formed by spin-coating at 3000 rpm for 1 minute. The PI on the glass slide is then cured at 250°C for 2 hours. Subsequent to this process, E-beam deposition of Titanium or Gold (3 μm thickness) followed by photolithography defines the conducting traces. Then, a second layer (2 μm) of PI is deposited, serving as encapsulation

for making a mechanically neutral plane. PI/metal/PI layers are then etched into serpentine-shaped structures using photolithography and reactive ion etching.

After this process, the circuit components – micro-LEDs, capacitors, resistors, and inductors – are then placed onto the designated etched areas with soldering paste. At this time, the matching capacitance value is determined for the operating frequency which is 13.56MHz for the devices described subsequently. First, a Series Network Analyzer measures the impedance value (L_m) of the attached device at the frequency of interest. Then, solving

$$L_a = \frac{1}{\left(\frac{1}{L_m}\right) + (\omega^2 C_c)} \tag{1}$$

where $L_a$is the matching inductance, L_m is the matching impedance calculated in the previous step, C_c is the device's capacitance, and ω is the resonant angular frequency. After calculating L_a, the matching capacitance can be determined by

$$C_m = \frac{1}{\omega^2 L_a} \tag{2}$$

where L_a is the matching inductance, and $C_m$is the matching capacitance. Proceeding this calculation, an approximately equal capacitor is soldered to the specified location.

In order to electrically bond the LEDs and device components to the conductive traces, the glass substrate is then cured at 250°C in a vacuum oven for 10 minutes. Next, the device is spin-coated with PDMS and cured at 70°C for 1 hour. Lastly, the device is separated from the glass substrate and PMMA is dissolved in acetone.

Single-Channel Light Emitting Device

Circuit and Antenna Design

The single-channel device features a micro-LED and a large capacitor for power storage. In conjunction, the design permits single-neuron activation for short-term experiments

unrestricted by antenna power transmission limitations. The device is composed of a Schottky Diode, a micro-LED, a capacitor (labelled Cvariable in figure 1), an antenna, and RF matching capacitors (labelled Cmatching in figure 1).

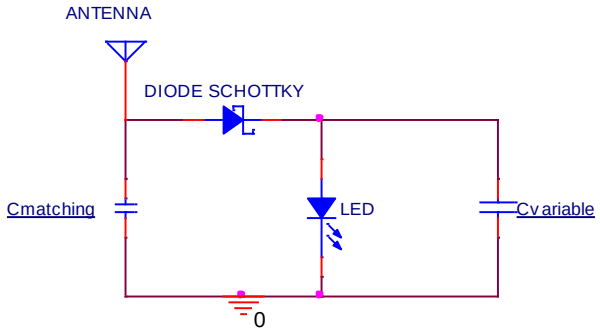

Figure 1. Circuit design of Single-Channel Optoelectronic Device

Located between the power source and the loads, the Schottky Diode permits current flow if the power source supplies greater than 150-450mV. Operating at 13.56MHz, an outside RF transmission antenna magnetically couples with the device's receiving antenna. The Schottky diode then rectifies the RF signal to generate a current source to power the micro-LED and charge the capacitor.

Device Fabrication

Using the techniques described in "Device Fabrication", devices capable of emitting light from a single micro-LED were fabricated with capacitance of 11mF, 22mF, or 91mF. Figure 2 below depicts the device with 91mF capacitance such that CPH3225A is an 11mF capacitor.

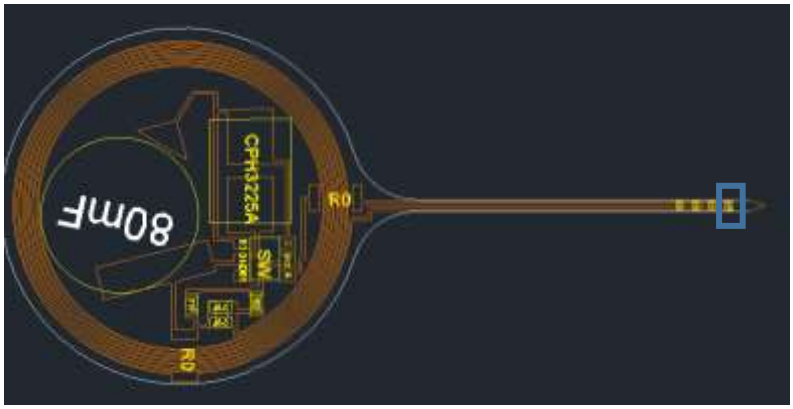

Figure 2. Complete single-channel device design utilizing 91mF capacitance.

By omitting the 80mF capacitor displayed in Figure 3, the device contains 11mF. Similarly, by replacing the 80mF capacitor with an 11mF capacitor, the device supports 22mF. During the experiment, the switch, indicated by SW in Figure 3, was removed.

During experimentation, a single blue micro-LED was attached at the location indicated by the blue box shown in figure 2. The micro-LED's operates within a voltage range of 2.7V to 3.1V according to the provided specifications sheet. Figure 3 depicts the operating range of the micro-LED.

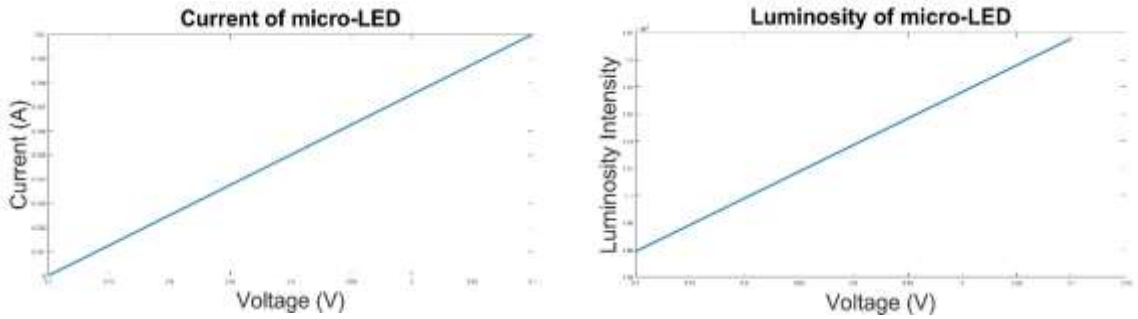

Figure 3. A) Luminosity of micro-LED. B) Current versus voltage curve of the micro-LED.

Testing Charging and Discharging of Capacitors

For optimization, the single-channel device was then tested using the following variables: capacitance, RF power magnitude, RF power frequency, and location in experiment cage. To determine the device performance in relationship to capacitance, three devices for capacitance values of 11mF, 22mF, and 91mF were fabricated.

An OBID RFID reader tunes the transmitting antenna to function at 13.56MHz and generate DC power. When tuned, the antenna capacitance values were $C_{1/1}$ and $C_{1/2}$ equal to 56pF, C_2 equal to 8pF, and Phi (ϕ) equal to 2° permitting the antennas real impedance to total 50Ω. Controlled through ID ISOStart 2017, the OBID RFID Reader was programmed with power ranging from low to 8W. Additionally, the OBID RFID Reader was programmed to pulse

on and off at 2Hz, 1Hz, and 0.67Hz. Figure 4 represents a pulse sequences in which the RF pulse is modulated at varying frequencies.

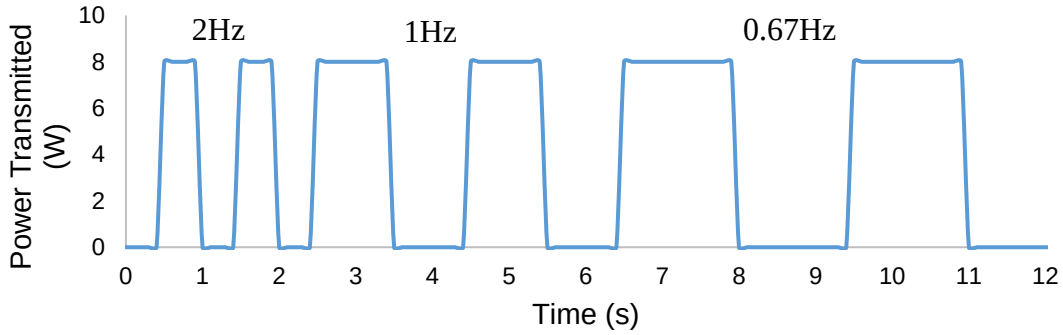

Figure 4. Power output of OBID RFID Reader programmed to modulate RF pulse frequency.

Lastly, the device's functionality was observed at five locations, Center, Left Top, Right Top, Left Bottom, and Right Bottom, in the experiment cage (figure 5A). By observing the variance in light intensity and charge time, the relationship between the strength of the magnetic field and the distance from the TX antenna was established. Figure 5B depicts the setup of the transmitting antenna utilized during the experiment.

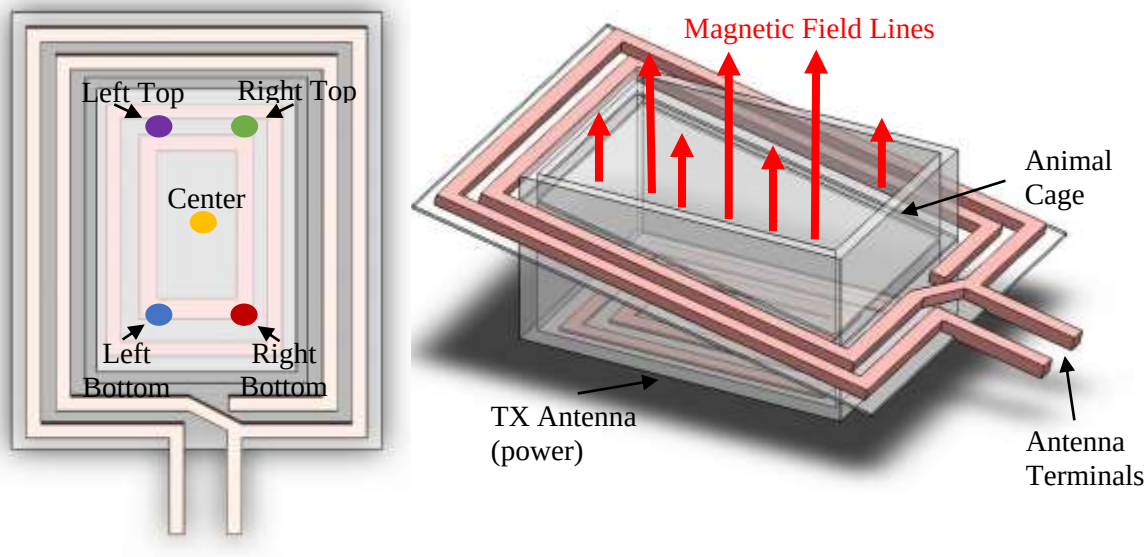

Figure 5. A) Locations of data collection in experiment cage.
B) Experiment cage with TX antenna.

The final feature of the single-channel device is the RF receiving antenna shown looping around the components in figure 2. A serpentine coil encompasses the device, permitting a wide range of motion, while receiving RF transferred power through magnetic coupling at 13.56MHz to the RF transmission loop antenna displayed in figure 5. As a result, the device is powered wirelessly by harvesting RF energy.

Multi-Channel Light Emitting Device

Circuit Design

The multi-channel device includes a RF receiving antenna similar to that used by the single-channel device. Again, the RF transmission loop antenna operating at 13.56MHz emits power which is transferred through capacitive coupling to the receiving antenna which surrounds the device. Although not displayed in figure 6, the receiving antenna encompasses the entire circuit shown in the image and is composed of serpentine coils. Upon receiving the RF transmitted power, a low-noise LDO regulator, labelled as MIC5205 in figure 6, controls and linearizes the transmitted voltage.

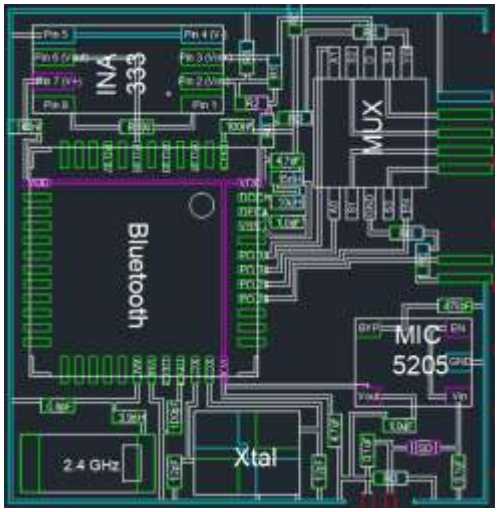

Figure 6. Multi-channel device schematic.

Functioning to consecutively choose one of four inputs, the MUX selects a channel, either S1, S2, S3, or S4, using logic from A0 and A1 to control the selection. This selection

results in two alterations. First, a micro-LED corresponding to the chosen channel emits light. Second, the channel acquires the signal generated from the activation or inhibition of the neuron. After acquiring the desired signal, the voltage is passed to INA 333, a micro-power instrumentation amplifier, with a gain of 10,000. This voltage is collected for future analysis. Upon selecting a different input using MUX logic, the aforementioned is repeated for the newly channel of interest.

LED Control System

To enable multi-channel light emission from a single device at variable frequency, Keil uVision5 software was used to program a nRF52832 Bluetooth chip. To confirm validity of the program, a nRF52 Development Kit hosting a nRF52832 Bluetooth chip was used.

CHAPTER III

RESULTS

As a result of the experiments, the single-channel device, multi-channel device, and transmitted and receiving antennas receive full characterization. Furthermore, the operational parameters attained permit equations which describe the device's function and can predict optimal performance.

Optimization of Single-Channel Device

Experimentation utilizing variable parameters permits the characterization, including charging and discharging times, of the single-channel device. The parameters investigated, including variable capacitance (11mF, 22mF, and 91mF, refer to figure 7), RF power magnitudes (low power, < 2W, and 8W), and RF power frequencies (2Hz, 1Hz, and 0.67Hz), allow for comprehension of the device's functional boundaries which synthesized allow for optimal performance. Formulated by synthesizing the above-mentioned boundaries, equations for internal resistance, charging, and discharging describe the device's functionality. Lastly, the performance of the receiving and transmitting antennas provide knowledge of the RF power transmission efficiency across the experiment chamber.

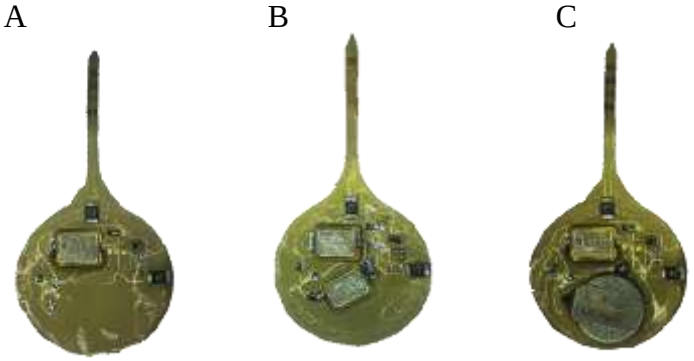

Figure 7. Single-channel optoelectric devices supporting A) 11mF device. B) 22mF device. C) 91mF device

Charging Characterization of Device

The device's charging characterization involves testing with variable capacitance (11mF, 22mF, and 91mF), RF power (Low Power, and 8W), RF frequency (2Hz, 1Hz, and 0.67Hz), and location in the experiment chamber (Left Top, Right Top, Left Bottom, Right Bottom, Center – refer to figure 5A). Such characterization permits comprehensive understanding of the functional limitations of the device. Figures 8-10 below depict the results.

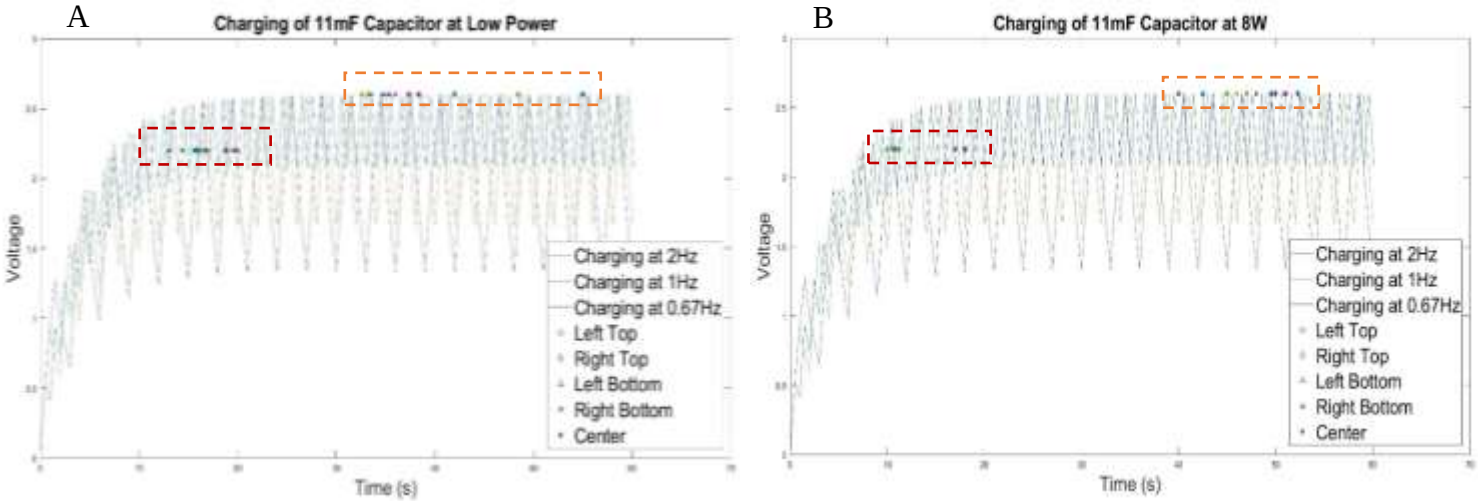

Figure 8. A) Charging of 11mF capacitance device at low power. B) Charging of 11mF capacitance device at 8W power. Markers in the red box indicate when the micro-LED initial emits light. Markers in the orange box indicate when the capacitor is fully charged.

Devices with 11mF capacitance display charging time variation as a result of location in the experiment cage and the frequency of the RF power pulse. At low power, the frequency of the RF power source greatly impacts the time at which the micro-LED initially turns on. The inverse relationship of frequency and charging time remains true at lower power, refer to figure 8A. However, with the increased magnitude of RF power transmitted, the strong inverse relationship declines such that the initial LED light emission time for 0.67Hz and 1Hz approximately equal each other and remain shorter than for 2Hz light emission. Thus, independent of location in the experiment field, the inverse relationship of frequency and device charging time weakens with an increase in RF power transmitted. When charging at low power,

the average time for the 11mF device's micro-LED to initially emit light, independent of location, for 2Hz, 1Hz, and 0.67Hz equals, in order, 11.8s, 17.8s, and 18.8s with charge times of 41.3s, 37.9s, and 36.9s. At 8Ws, the initially time for light emission operating at 2Hz, 1Hz, and 0.67Hz equals 10.9s, 10.3s, and 17.0s, whereas the charging time equals 47.3s, 45.6s, and 47.2s.

The performance of the antenna also operated with biases to the power transmitted. At low power, devices located in the center of the experiment chamber receive inadequate power to emit light from the micro-LED regardless of RF power frequency. When power is increase to 8Ws, however, the device functions at all locations in the experiment cage. As such, it can be inferred that at low power, the threshold voltage for light emission, approximately 2.12Volts, is not reached. Comparison of device performance in varying locations provides additional insight into antenna efficiency. At locations closest to the antenna terminals (Left and Right Bottom), the device charges most quickly, initially emitting light several seconds earlier than other locations. Additionally, when charging at higher power, the charging time appears more dependent upon the location of the device in the chamber than the frequency of the RF power pulse as depicted in figure 8B.

Devices with 22mF capacitance displayed similar effects to those of the 11mF devices operating under the same conditions. At low power, the highest frequency, 2Hz, corresponds to the shortest time for initial micro-LED light emission and to reach full power. Devices powered at 1Hz and 0.67Hz however, did not show distinction in the time for initial micro-LED light emission or for charging time.

While the frequency of the RF power remained influential on the charging time for low power, at 8W RF power, the RF power frequency bears little impact on either of these characteristics for 22mF capacitance devices as seen in Figure 9B. At higher frequency, the

device reaches full charge more quickly than at low frequency although the clear linear relationship shown in the charging of the 11mF is less precise. Again, devices located at the center of the chamber during charging at low RF power magnitude received insufficient voltage to emit light from the micro-LED.

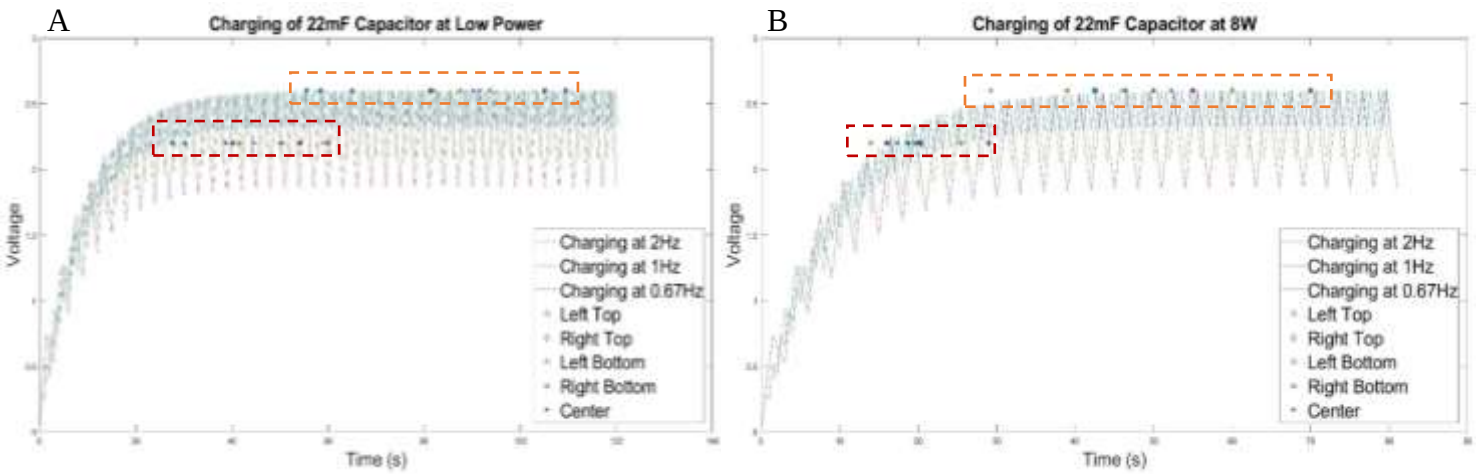

Figure 9. A) Charging of 22mF capacitance device at low power. B) Charging of 22mF capacitance device at 8W power. Markers in the red box indicate when the micro-LED initial emits light. Markers in the orange box indicate when the capacitor is fully charged.

In summary, at low power and 22mF capacitance, the average time for initial light emission from the micro-LED operating at 2Hz, 1Hz, and 0.67Hz equals 35.3s, 47.9s, 51.4s with charging times of 67.7s, 86.1s, and 98.7s. Charged at 8Ws, the average time for initial light emission decreases to 21.1s, 19.1s, and 23.0s, and the charging time decreases to 48.4s, 39.7s, and 73.0s.

The characteristics discussed above remain true for the device supporting 91mF capacitance as shown in figure 10. When charging a 91mF capacitance device at low power, the RF power frequency only decreased the initial light emission time and charging time for devices located in the area closest to the input terminal of the antenna. Devices powered at low power

and low frequency or 8W showed no differentiation in charging time in relation to location in experiment chamber.

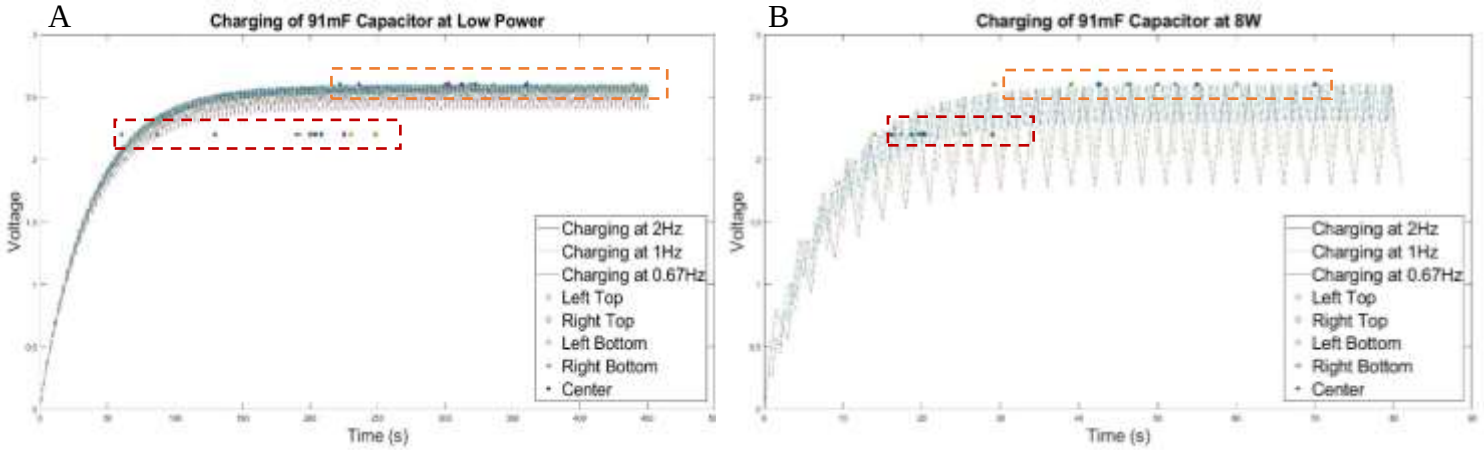

Figure 10. A) Charging of 91mF capacitance device at low power. B) Charging of 91mF capacitance device at 8W power. Markers on the left show when the micro-LED initial lights up. Markers on the right show when the capacitor is fully charged.

While charging at low power, a device with 91mF capacitance averages initial light emission times of 139.0s, 218.1s, and 189.8s when operating at 2Hz, 1Hz, and 0.67Hz respectively. The device charging times equal 316.5s, 349.6s, and 283.2s under RF power frequency of 2Hz, 1Hz, and 0.67Hz. When charged at 8Ws, the average time for initial light emission reduces to 47.8s, 62.6s, and 74.8s, and the charging time decreases to 99.9s, 116.7s, and 108.2s.

The device's charging characteristics can be further described by

$$V(t) = V_s\left(1 - e^{-\frac{t}{(200\ \Omega)(C\ mF)}}\right) \tag{3}$$

where V_s is the voltage of the source, t is time, and C is the capacitance. The device's internal resistance approximately equals 200Ω. While charging, the Schottky diode and micro-LED (refer to figure 1) function in forward bias and contribute 195.32Ω in series with 4.68Ω contributed by the device's Copper wiring calculated using

$$R = \rho\frac{L}{A} \tag{4}$$

in which ρ is the resistivity of Copper, *L* is the length of the Copper channel, and *A* is the area of the Copper channel. Therefore, the device's time constants equal $\tau_{C=11mF} = 2.2\ seconds$, $\tau_{C=22mF} = 4.4\ seconds$, and $\tau_{C=91mF} = 18.2\ seconds$ for the charging of the device.

Discharging of Capacitors

In order to increase the versatility of experimentation, the device must hold charge for an extended period of time. The device is characterized for capacitance values of 11mF, 22mF, and 91mF. Due to the Schottky diode and micro-LED functioning near the forward junction potential, the resistance of the circuit increases substantially from that calculated during the charging of the device. Devices charged at varying locations within the experiment cage were proven to reach equivalent capacitance charge. As expected, the device's discharging time is approximately equal regardless of charging location.

Supporting 11mF capacitance, the device's resistance is calculated from the conducted experiments as averaging 272.09kΩ. The discharging equation is

$$V_{11mF}(t) = V_s e^{-\frac{t}{(272k\Omega)(11mF)}} \quad (5)$$

where V_s is the voltage of the source and t is time. The time constant, τ_{11mF}, equals 49.883 minutes.

All 11mF devices share an approximately equal time at which the LED no longer emits light, 11.89 minutes, proving the devices reach full charge from any location in the experiment chamber. Applying equation 4 to the data collected for 11mF capacitance at all locations produces a sum of squared errors of prediction (SSE) of 4.334×10^{-4}, an R-squared value of 0.999, and root mean square error (RMSE) of 0.019. Therefore, the above equation accurately predicts the discharging characteristics of a device with 11mF capacitance.

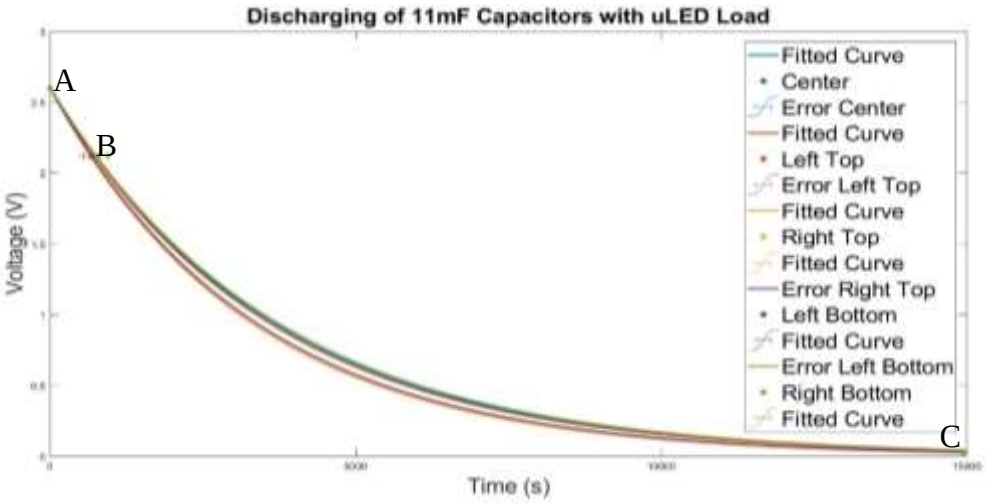

Figure 11. Discharging of 11mF Capacitor with micro-LED load. Point A indicates initial voltage after remove from the power supply. Point B displays when the LED no long emits visible light. Point C indicates when the capacitor is fully discharged. Standard error calculated from experimental results and fitted equations prediction is shown.

Figure 11 synthesizes the abovementioned results and confirms the validity of equation 5.

Reiterated trials permit the confirmation of the device's discharging characteristics for 22mF capacitance as shown in figure 12. All 22mF devices share approximately equal discharging times, averaging 22.442 minutes, proving the devices reach full charge from all location in the experiment cage.

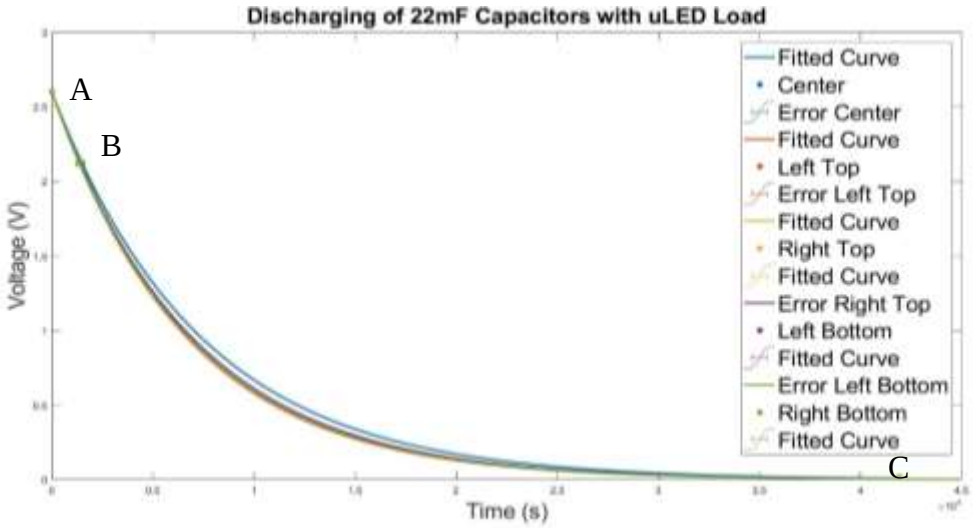

Figure 12. Discharging of 22mF Capacitor with micro-LED load. Point A indicates initial voltage after remove from the power supply. Point B displays when the LED no long emits visible light. Point C indicates when the capacitor is fully discharged. Standard error calculated from experimental results and fitted equations prediction is shown.

Experimentation determines that the average resistance of a device with 22mF capacitance equals 380.93kΩ. As such, the discharging equation is

$$V_{22mF}(t) = V_s e^{-\frac{t}{(381k\Omega)(22mF)}} \quad (6)$$

where V_s is the voltage of the source and t is time. The time constant, τ_{22mF}, equals 2.327 hours.

Computing the goodness of fit for equation 5 for data collected for 22mF capacitance at all locations yields an SSE of 1.319×10^{-4}, an R-squared equal to 1.000, and an RMSE of 0.011. Therefore, equation 5 is an accurate discharging equation for a single-channel device supporting 22mF capacitance.

A device including 91mF capacitance contains an average internal resistance of 212.89kΩ. Therefore, the discharging equation is

$$V_{91mF}(t) = V_s e^{-\frac{t}{(213k\Omega)(91mF)}} \quad (7)$$

where V_s is the voltage of the source and t is time. Accordingly, the time constant equals τ_{91mF}, 5.381 hours. Figure 13 below shows the experimental results of the discharging of the devices and their alignment with the equal formulated above.

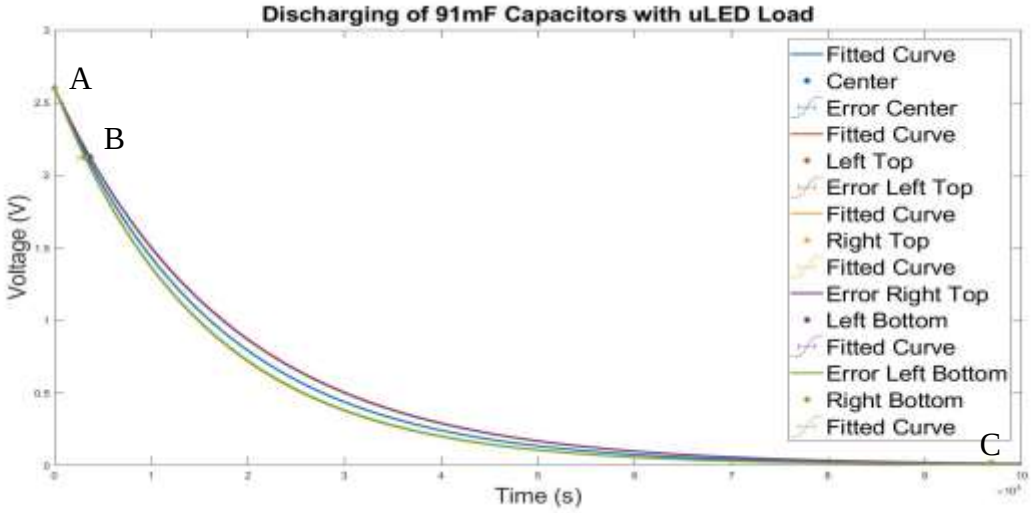

Figure 13. Discharging of 91mF Capacitor with micro-LED load. Point A indicates initial voltage after remove from the power supply. Point B displays when the LED no long emits visible light. Point C indicates when the capacitor is fully discharged. Standard error calculated from experimental results and fitted equations prediction is shown.

All 91mF devices share equal discharging times, again showing the devices reach full charge from any location in the experiment chamber. Calculating goodness of fit for equation 6, the SSE is 0.0172, R-square is 0.995, and RMSE is 0.130. Although the fit of equation 6 for 91mF capacitance is not as good as equations 4 for 11mF and equation 5 for 22mF, the equation still accurately predicts the discharging time for a device carrying 91mF capacitance.

Controlled for the device fabrication and component variability, the internal resistance of the device must approximately match regardless of the capacitance. Therefore, the total device resistance equals 288.636kΩ.

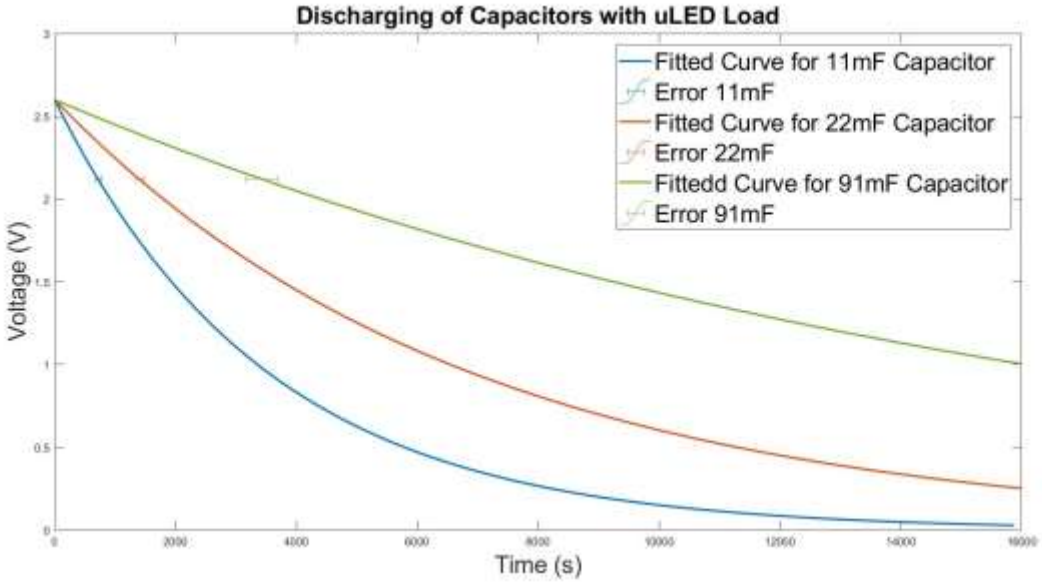

Figure 14. Discharging of 11mF, 22mF, and 91mF capacitor with micro-LED load. Standard error calculated from experimental results and fitted equations prediction is shown.

Therefore, the final discharging equation for the single-channel device is

$$V_C(t) = V_s e^{-\frac{t}{(288.636k\Omega)(C\ mF)}} \tag{8}$$

where V_s is the voltage of the source, t is time, and C is the capacitance. The above equation is plotted in figure 14 for capacitance values of 11mF, 22mF, and 91mF. Applying the above equation to the data collected for 11mF capacitance produces a SSE of 1.296×10^{-4}, an R-squared value of 1, and RMSE of 0.0114. Similarly, when applying equation 7 to the

experimental results of discharging a 22mF device, the error is minimal. For 22mF, the SSE is 6.514×10^{-5}, R-squared value is 1, and RMSE is 0.0081. Lastly, the results of applying equation 7 to devices of 91mF capacitance produce insignificant error although slightly larger than that of 11mF and 22mF applications. Comparing averaged experimental results from all locations to fitted predictions for 91mF capacitance results in an SSE of 2.723×10^{-4}, an R-squared value of $0.99\bar{9}$, and an RMSE value of 0.0165.

The close alignment with experiment results supports the conclusion that equation 7 correctly portrays the discharging characteristics of the single-channel device with minimal error. As the total resistance of the device equals 288.636kΩ and the device's Copper wiring resistance equals 4.68Ω, the circuit's Schottky diode and micro-LED function close to the forward junction potential and contribute 288.634kΩ.

However, equation 2 and equation 7 over simplify the characteristics of the Schottky diode and micro-LED as a diode's resistance is non-linear, but rather determined by the current-voltage relationship.

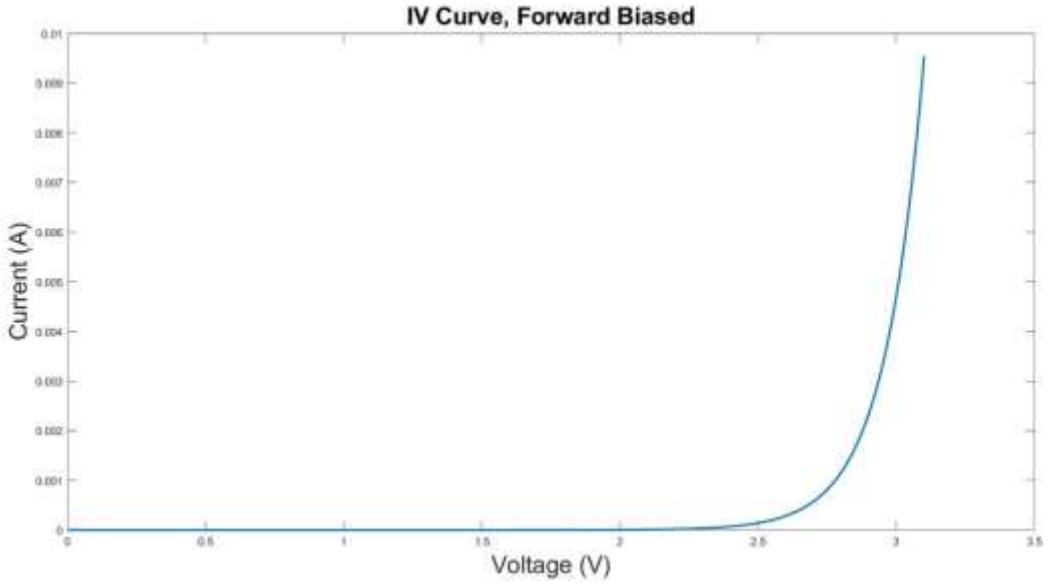

Figure 15. Current-Voltage relationship of the single-channel device in the forward direction.

Using the previous calculations, the circuit's current-voltage relationship in forward bias is described by Figure 15 above. This relationship can also be described by

$$I(V) = 1.214 \times 10^{-16} e^{10.33V} \quad (9)$$

where *V* is the voltage applied across the diode, and *I* is the current through the diode. Knee voltage of the diode is calculated as 2.12V. The fitted curve has an SSE of 1.189×10^{-6}, an R-square of 0.900, and an RMSE of 5.453×10^{-4}. As such, equation 8 accurately describes the current-voltage relationship of the diode components in the single-channel device. The resistance, *R*, at current, *I*, can then be calculated by

$$R(I) = 0.142 I^{-1} \quad (10)$$

Therefore, the calculation of the discharging and charging of the device is accurately evaluated by introducing a voltage dependent time constant ($\tau = RC$) as described in figure 16 and equation 10.

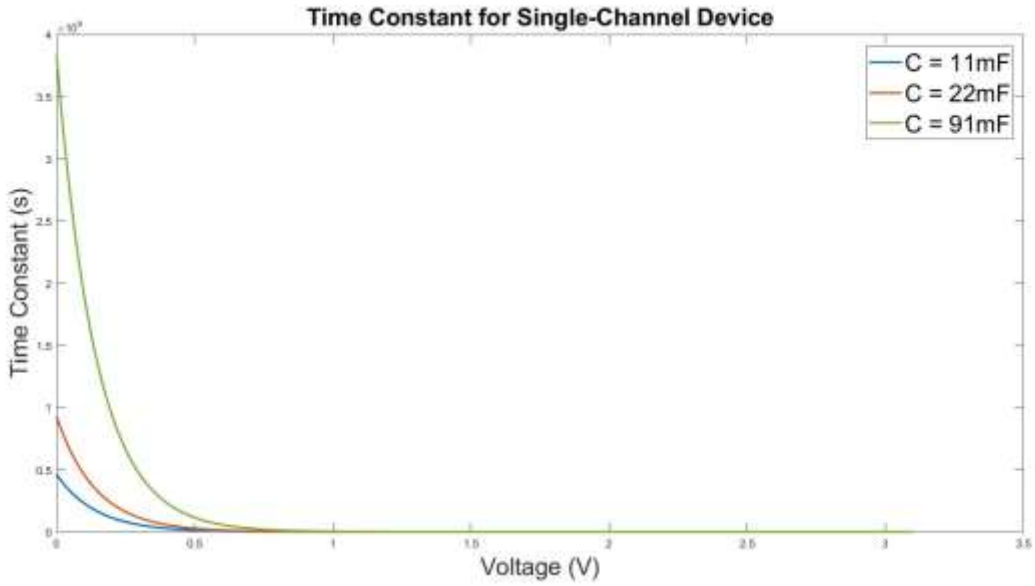

Figure 16. Time constant for Single-Channel Device at 11mF, 22mF, and 91mF capacitance.

The equation for the charging of the single-channel device at variable capacitance is

$$V_C(t) = V_s\left(1 - e^{-\frac{t}{\left(\frac{0.142}{I(t-1)}\Omega\right)(C\ mF)}}\right) \tag{11}$$

$$= V_s\left(1 - e^{-\frac{t}{\left(\frac{0.142}{1.214\times10^{-16}e^{10.33V_C}}\Omega\right)(C\ mF)}}\right)$$

where V_c is the voltage across the capacitor, V_s is the voltage of the source, t is time, and C is the capacitance. This equation, however is a first-order difference equation and must be constrained by the auxiliary conditions $V_c(t_0) = 0\ for\ t_0 < 0$. Additionally, the equation for the discharging of the single-channel device at variable capacitance is

$$V_C(t) = V_s e^{-\frac{t}{\left(\frac{100}{307I}\Omega\right)(C\ mF)}} = V_s e^{e^{-\frac{t}{\left(\frac{0.142}{1.214\times10^{-16}e^{10.33V_C}}\Omega\right)(C\ mF)}}} \tag{12}$$

where V_c is the voltage across the capacitor, V_s is the voltage of the source, t is time, and C is the capacitance. Similar to the charging equation, equation 11 represents a first-order difference equation and must be subject to auxiliary conditions $V_c(t_0) = V_s\ for\ t_0 < 0$.

Transmitting and Receiving Antenna Characterization

The study of the single-channel device's performance permits an examination of the transmitting and receiving antenna's efficiency and operational characteristics. At low power, the device's charging time shows greater dependence upon the position of the device in the experiment chamber regardless of the capacitance. Devices positioned close to the terminals of

the antenna, indicated in figure 17 as Left Bottom and Right Bottom, charge the fastest.

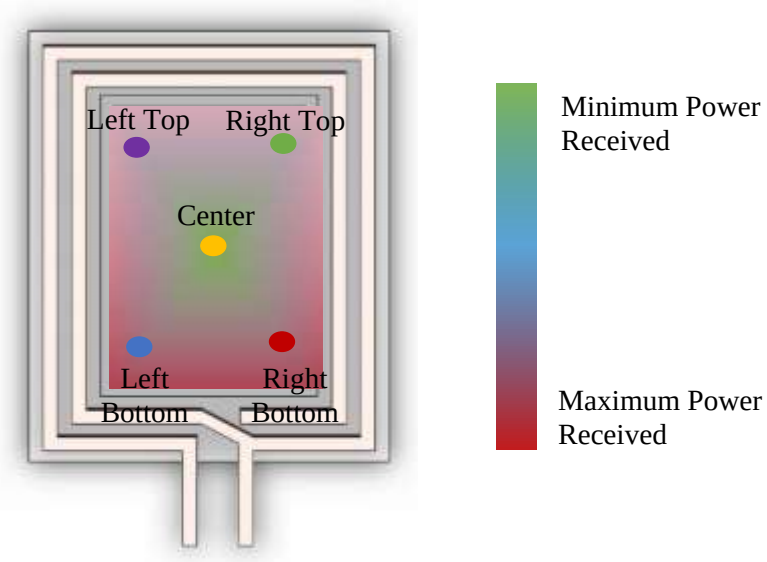

Figure 17. RF power strength across experiment cage.

The second largest magnitude of RF power is received in the Right and Left Top corners of the chamber. Devices placed in the center of the experiment chamber, however, receive lowest RF power transmission. These results exhibit nonhomogeneous power distribution across the experiment area. RF power reception varies with location in the chamber as characterized by the coloration of the experiment cage in Figure 17, consistent with experiments conducted previously (Cannon, Hoburg and Stancil).

A common expression for the power received by the antenna, the Friis equation denotes the dependent relationship of the power transferred to the antennas' effective area, the distance of separation between the antennas, and the wavelength of the RF power source. This relationship can be stated as

$$P_r = P_t \frac{(A_r A_t)}{(d^2 \lambda^2)} \tag{13}$$

where P_t is the power transmitted, P_r is the power received, A_t is the effective area of the transmitting antenna, $A_r$is the effective area of the receiving antenna, d is the distance between

antennas, and λ is the wavelength of the radio frequency. The results shown in figure 17 agree with the Friis equation. During the experiment, the effective areas and wavelength are held constant limiting the ratio of power transfer to power received as dependent upon the distance of the antennas, *d*.

LED Control System for Multi-Channel Device

The program designed in Keil uVision5 regulates the use of four channels on the multi-channel device. When a specific channel is selected, the device, simulated using the nRF52 Development Kit, will emit light from the corresponding LED, channel 1. At this time, the device also reads information from an assigned port in the Development Kit. Completing the period, the program selects channel 2. Again, the device emits light from channel 2's related LED and reads information from the output. Upon completing the period, the program cycles through channel 3, then 4, and final repeats to the top of the rotation.

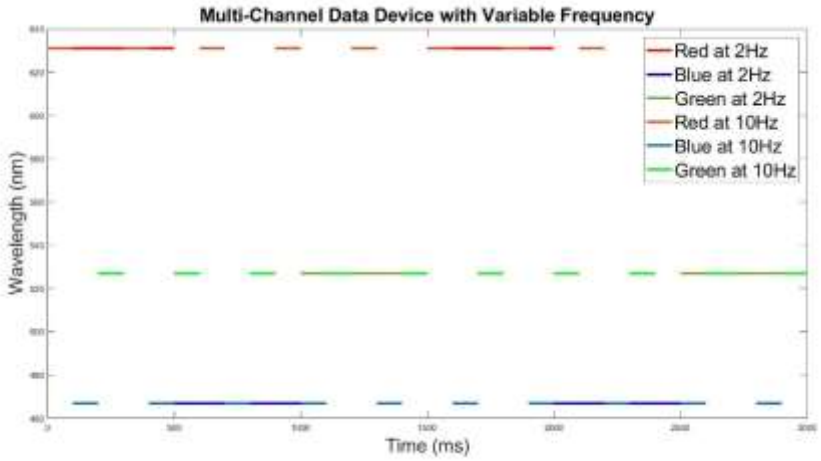

Figure 18. Example of frequency sequence generated from program.

The frequency of the cyclical lighting of four LEDs can be increased or decreased. Figure 18 depicts an example of a frequency program where the frequency equals 2Hz or 10Hz. This software program can later be used to collect one of four neural probe signals based upon the selected channel. This signal is then amplified for future analysis.

CHAPTER IV

DISCUSSION

Although the results of the experimentation provide insight into the device functionality, to most accurately understand the results, optimization of antenna efficiency must occur. Antenna efficiency is calculated by

$$e_t = e_r e_c e_d \tag{14}$$

where e_t= 1 for a lossless antenna, e_r measures reflection or matching efficiency, and e_c and e_d measure Ohmic losses where the former is for conductive losses and the latter measures dielectric losses (H. Matsner). In the experiment, the matching efficiency (e_r) varied dependent upon the matching capacitance calculated and applied in the circuit. Devices with optimal matching capacitance therefore received a higher portion of transmitted power, slightly altering the device's charging time. In order to improve the characterization of the device, all tested devices must perform with approximately equivalent efficiency (e_t).

CHAPTER V

CONCLUSION

Subject to biological and technological constraints, the application of optogenetics to study neural mechanisms encompasses multiple dimensions. As a result, device limitations on all fronts must be comprehended and overcome to improve functionality. During this study, we evaluated optoelectronic devices' performance under several conditions and introduced new device designs.

Testing under conditions of variable RF power magnitude, RF power frequency, capacitance, and locations in the experiment cage characterized the single-channel device's performance and provided insight into antenna efficiency. Experimental results show that as capacitance and RF power increases, the time required to charge the device's capacitor becomes independent of the device's location in the experiment chamber and of the RF power frequency. However, at low power, the devices located closest to the antenna, specifically near the antenna's terminals, received a larger portion of the power transferred in agreement with the Friis equation. Additionally, the micro-LED mounted on the device initially emits light at a time inversely proportional to the transmitted RF power's frequency regardless of capacitance or RF power magnitude.

The average discharging time for the single-channel device of 11mF, 22mF, and 91mF capacitance in order equals 11.89 minutes, 22.44 minutes, and 57.79 minutes. In addition, a non-linear relationship describes the device's current-voltage relationship, explaining the large change in resistance found between charging and discharging. Therefore, the charging and

discharging equations describing the device include an exponential value of resistance dependent upon the previous voltage value.

Along with the characterization of the single-channel device, we appraised a multi-channel device's design and functionality. Through this work, a program for controlling the selected channel of a multi-channel device was written. This program permits channel selection at a user specified frequency. For this period, the selected channel emits light from a corresponding micro-LED and collects information from the stimulated neuron.

As a result of device characterization, performance may be optimized to satisfy experimental conditions. For example, if an experiment requires the mouse to perform an activity outside of the antenna area, an optimal capacitance value can be determined to extend trial's duration. In order to increase understanding of the device constraints, additional experiments should be performed to calculate the antenna's efficiency. Benefit would also come from developing a method to measure the micro-LED's luminosity while within the antenna to improve the accuracy of calculated charging time.

With the expansion of optoelectronics, human understanding of neural activity will proportionally grow. Permitting highly controlled targeting of regions of interest, optoelectronics advances our knowledge of neural circuitry in animals, unparalleled by previous methods. In order to capitalize on the full potential of the technology, device parameterization is imperative. Although hardly scratching the surface of full characterization, the work discussed in the previous pages permits insight into possible experiments and the huge potential of optoelectronics.

REFERENCES

Aravanis AM, Wang LP, Zhang F, Meltzer LA, Mogri MZ, Schneider MB, Deisseroth K. "An optical neural interface: in vivo control of rodent motor cortex with integrated fiberoptic and optogenetic technology." *Journal of Neural Engineering* (2007): 143-56.

Cannon, B.L., et al. "Magnetic resonant coupling as a potential means for wireless power transfer to multiple small receivers." *IEEE Trans. Power Electron* (2009): 1819-1824.

Gunchul Shin, Adrian M. Gomez, Ream Al-Hasani, Jeong Sook Ha, Michael R. Bruchas, John A. Rogers. "Flexible Near-Field Wireless Optoelectronics as Subdermal Implants for Broad Applications in Optogenetics." *Neuron* (2017): 509-521.

Guru, Akash, et al. "Making Sense of Optogenetics." *International Journal of Neuropsychopharmacology* (2015).

H. Matsner, S. Levy. *Antenna Gain*. 15 July 2004. 20 March 2018.

Rost, Benjamin, et al. "Optogenetic Tools for Subcellular Applications in Neuroscience." *Neuron* (2017): 572-603. Volume.

Sung Il Park, Daniel S Brener, John Rogers. "Soft, stretchable, fully implantable miniaturized optoelectronic systems for wireless optogenetics." *Nature Biotechnology 33* (2015): 1280-1286.

Sung Il Park, Gunchul Shin, Jordan G. McCall, Ream Al-Hasani, Aaron Norris, Li Xia, Daniel S. Brenner, Kyung Nim Noh, Sang Yun Bang, Dionnet L. Bhatti, Kyung-In Jang, Seung-Kyun Kang, Aaron D. Mickle, Gregory Dussor, Theodore J. Price, Robert W. Gereau, M. "Stretchable multichannel antennas in soft wireless optoelectronic implants for optogenetics." *Proceedings of the National Academy of Sciences of the United States of America* (2016): 8169-8177.